Journal of Solid State Chemistry 181 (2008) 3229–3235

Contents lists available at ScienceDirect

Journal of Solid State Chemistry

journal homepage: www.elsevier.com/locate/jssc

Ab-initio crystal structure of hydroxy adipate of nickel and hydroxy subarate of nickel and cobalt from synchrotron powder diffraction and magnetic properties

Adel Mesbah [a], Anne Carton [a], Lionel Aranda [a], Thomas Mazet [a], Florence Porcher [b], Michel François [a,*]

[a] Laboratoire de Chimie du Solide Minéral, UMR 7555, Université Henri Poincaré, F-54506 Vandoeuvre les Nancy, France
[b] Laboratoire de Cristallographie et de Modélisation des Matériaux Minéraux et Biologiques, UMR UHP–CNRS no 7036, Université Henri Poincaré, Nancy I, 54506 Vandoeuvre les Nancy, France

ARTICLE INFO

Article history:
Received 22 February 2008
Received in revised form
27 June 2008
Accepted 29 June 2008
Available online 23 August 2008

Keywords:
Hybrid compound
Crystal structure
Rietveld analysis
Magnetic properties

ABSTRACT

Organic–inorganic hybrid compounds $Ni(II)_5(OH)_6(C_6H_8O_4)_2$ **(1)**, $Ni(II)_5(OH)_6(C_8H_{12}O_4)_2$ **(2)** and $Co(II)_5(OH)_6(C_8H_{12}O_4)_2$ **(3)** have a similar layered structure as determined *ab initio* from synchrotron powder diffraction analysis. The metal sites are octahedrally coordinated by O atoms. The slabs are built from edge-sharing octahedra in such a way that channels with an average size of 4 Å are formed. Bis-bidentate and bridging dicarboxylate anions lead to a 3D framework. The compounds **(1)** and **(2)** order antiferromagnetically below $T_N = 26.5$ and 19.3 K, respectively, while **(3)** is ferrimagnetic with $T_C = 16.2$ K. Crystal data for compounds are as follows: **(1)** $a = 11.6504(1)$ Å, $b = 6.8021(3)$ Å, $c = 6.3603(1)$ Å, $\alpha = 73.52(1)^\circ$, $\beta = 99.69(1)^\circ$, $\gamma = 96.16(1)^\circ$, $R_B = 0.070$, 668 reflections; **(2)** $a = 13.9325(1)$ Å, $b = 6.7893(1)$ Å, $c = 6.3534(4)$ Å, $\alpha = 73.63(1)^\circ$, $\beta = 95.14(1)^\circ$, $\gamma = 91.80(1)^\circ$, $R_B = 0.052$, 804 reflections; **(3)** $a = 13.9806(1)$ Å, $b = 6.9588(1)$ Å, $c = 6.3967(1)$ Å, $\alpha = 73.05(1)^\circ$, $\beta = 94.51(1)^\circ$, $\gamma = 92.19(1)^\circ$, $R_B = 0.048$, 410 reflections. The space group is $P-1$ for the three compounds.

1. Introduction

Over the past two decades, hybrid metal-organic materials have been intensively investigated, with a particular interest for the magnetic, optical and electrical properties associated with the various crystallographic structures. A recent review article surveys the progress that has been made on this subject [1]. As these metal-organic compounds often consist of more or less open or porous networks, these materials also find application as catalysts or for gas adsorption applications [2–5]. Among these compounds, those based on carboxylates are of particular interest. Review papers have been published that discuss the structural properties and strategies of chemical synthesis [6], magnetic properties, etc. [7]. Another one, focused especially on cobalt and nickel carboxylates [8], is also available.

In this paper, we investigated hybrid compounds based on dicarboxylate linkers for several reasons. These compounds can be synthesized easily under mild conditions of temperature and pressure and are thermally stable up to 400 °C. The dicarboxylates tend to form highly crystalline products. This facilitates the determination of their crystallographic structures more accurately than in the corresponding monocarboxylates. Moreover, due to the covalent bonds between the organic and mineral network, it is possible to imagine coupling between the properties of the two sub-networks. For example, it was shown that in Ni(II)-layered organic–inorganic compounds, the magnetic properties of the layers of nickel hydroxide influence the optical properties of the grafted luminescent molecules [9].

These compounds are synthesized in basic media to support the presence of hydroxides. *M* is a divalent transition metal element from the first series of the Periodic Table. The crystal structures of many such compounds have been accurately determined. In most cases the metal is located exclusively in an octahedral site, coordinated by O [10–26]. The oxygen atoms usually come from the hydroxide and/or carboxylate groups, but in some cases they come from the water molecules. The octahedra are connected via edge- or corner-sharing, which often leads to the formation of 1D chains [10–15] or 2D planes [16–25]. In the latter case, the planes can leave holes leading to porous materials [20,25]. Less frequently, the connection of the octahedra may lead to 3D networks [26].

This work attempts to contribute toward the development of new compounds in the *M*(II)-OH/dicarboxylates system. The main goal was to establish relations between the crystal structure and magnetic properties in the entitled compounds. The magnetism of the metal hydroxycarboxylates is relatively well understood [7,27] for compounds where the metal hydroxide layers form a brucite-like structure. In metal-hydroxy-dicarboxylates where the mineral

* Corresponding author. Fax: +03 83 68 46 11.
E-mail address: Michel.francois@lcsm.uhp-nancy.fr (M. François).

0022-4596/$ - see front matter © 2008 Elsevier Inc. All rights reserved.
doi:10.1016/j.jssc.2008.06.059

sub-unit differs and does not adopt a brucite-like arrangement, the magnetic behaviors are less well understood. For example, one can find ferrimagnetic compounds with 'chains' [10,11,13] or 'planes' [20,24,25,28], ferromagnetic compounds with 'planes' [19], antiferromagnetic compounds with 'chains' [14,15] or canted antiferromagnetics with 'planes' [16]. Conversely, the aforementioned compound with the 3D mineral network [26] remains paramagnetic at low temperature. In this work, three new compounds were synthesized by the hydrothermal route: Ni(II)5(OH)6(C6H8O4)2, Ni(II)5(OH)6(C8H12O4)2 and Co(II)5(OH)6(C8H12O4)2. Their crystal structures were determined from synchrotron X-ray powder diffraction (XRPD) measurements and their magnetic, optical and thermal properties are characterized.

2. Experimental

2.1. Synthesis, thermal and chemical analyses

The nickel hydroxy adipate $Ni(II)_5(OH)_6(C_6H_8O_4)_2$ **(1)** was synthesized by the hydrothermal route from a mixture (2:3) of $Ni(NO_3)_2 \cdot 2H_2O$ (Aldrich, 98%) and adipic acid $C_6H_8O_4H_2$ (Aldrich, 98%) in aqueous solution, typically $Ni(NO_3)_2 \cdot 2H_2O$ (1.50 g, 6.8 mmol), $C_6H_8O_4H_2$ (1.50 g, 10.3 mmol,). The pH of the solution was increased up to 8 by the addition of NaOH (0.1 M). About 20 ml of the starting mixture was homogenized and transferred into a 25 ml teflon-walled acid digestion bomb, and then heated under autogenous pressure for 72 h at 150 °C. The reaction product was collected by filtration, washed twice with a mixture of distilled water and anhydrous ethanol (1/1) and then dried at room temperature. The same procedure was applied for $Ni(II)_5(OH)_6(C_8H_{12}O_4)_2$ **(2)** with subaric acid $C_8H_{12}O_4H_2$ (Aldrich, 98%) (1.79 g, 10.3 mmol), $Ni(NO_3)_2 \cdot 2H_2O$ (1.50 g, 6.8 mmol) and for $Co(II)_5(OH)_6(C_8H_{12}O_4)_2$ **(3)** with subaric acid $C_8H_{12}O_4H_2$ (1.79 g, 10.3 mmol), $Co(NO_3)_2 \cdot 2H_2O$ (Aldrich, 98%) (1.50 g, 6.85 mmol).

Thermogravimetric (TG) measurements were performed with a 'TG/ATD 92–16.18' SETARAM instrument between 20 and 600 °C in air and using a heating rate of 1°/min. The thermal curves for **(1)**, **(2)** and **(3)** are reported in Fig. 1. For each compound the weight loss occurs in a single stage, at 320 °C for **(1)**, and at 300 °C for **(2)** and **(3)**. It is ascribed to the transformation from **(1)** or **(2)** to NiO (as determined by X-ray diffraction, PDF: 44–1159) (43.5% obs; 45.5% calc **(1)**, 48.5% obs; 47.5% calc **(2)**) and from **(3)** to CoO (PDF: 75–0533) (45.3% obs; 45.3% calc **(3)**).

Chemical analysis: **(3)** C (obs: 26.20%; calc 25.92%), Co (obs: 36.02%; calc 30.24%); H (obs: 4.08%; calc 4.05%).

2.2. IR and UV spectroscopy

The IR spectrum was recorded with a 'Spectrum one FT-IR' spectrometer (Perking Elmer Instrument) in the ATR mode using the 'Universal Sampling Accessory'.

UV–visible spectra were performed for compounds **(1)**, **(2)** and **(3)** with a CARY 4000 spectrometer operating in the 175–900 nm range.

2.3. Magnetic measurements

DC and AC magnetic susceptibility measurements were carried out with a PPMS Quantum Design [29], between 5 and 300 K for **(1)**, **(2)** and **(3)**. The χ_{DC} curves were recorded under a field of 10 kOe to determine the molar Curie constant (C_M), the paramagnetic Curie temperature (θp) and the effective moment (μ_{eff}). The χ_{AC} dependences with temperature were collected using a frequency of 100 Hz and alternative magnetic field $H_{AC} = 5$ Oe. No correction for diamagnetism was applied.

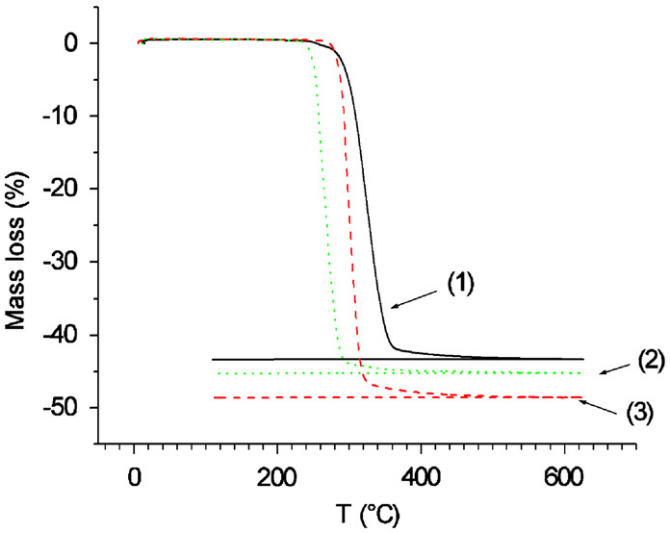

Fig. 1. TGA curve of **(1)**, **(2)** and **(3)**.

2.4. XRPD and ab-initio structure determination

XRPD data were collected at 100 K using synchrotron radiation (ESRF, ID 31, the transmission Debye Scherrer geometry). The diffractometer was equipped with a primary Si(111) double-crystal monochromator and nine sensitive linear position detectors with crystal analyzers [30]. The sample of a fine powder form was introduced in a Lindeman tube ($\Phi = 0.8$ mm). Data were recorded using a wave length of 0.85124 Å, in the 2θ range 4–60° with an interval of 0.003° and a total counting time of 2 h. Crystal data and structure refinement parameters are reported in Table 1.

2.4.1. Indexing

Standard peak search methods with Reflex program from Material Studio (MS) system software (Accelrys) [31] were used to locate the diffraction maxima; indexing was performed with the Xcell [32] program. For the three compounds, the solutions were found in the triclinic system aP. The lattice parameters, presented in Table 1, were refined by the Rietveld method.

2.4.2. Resolution

The three structures were solved in the space group $P-1$ applying optimization methods (parallel tempering) in the direct space, using the FOX program [33]. On the basis of thermal and chemical analyzes and expected density as well as UV–visible results (see hereafter), the asymmetric unit was filled for each model with three independent $M(II)O_6$ octahedra and one linear dicarboxylate molecule $C_6H_8O_4$ for **(1)**; $C_8H_{12}O_4$ for **(2)** and **(3)**—introduced as rigid bodies in the starting models without their H atoms. The optimization led to initial models in agreement with the chemical formulae $Ni(II)_5(OH)_6(C_6H_8O_4)_2$ for **(1)**, $Ni(II)_5(OH)_6(C_8H_{12}O_4)_2$ for **(2)** and $Co(II)_5(OH)_6(C_8H_{12}O_4)_2$ for **(3)**. All three structures contain three metallic sites ($M1$, $M2$ and $M3$) and seven O sites (4 O_{carb} and 3 O_{OH}); **(1)** contains six, whereas **(2)** and **(3)** contain eight C-sites, respectively. The $M1$ site is located in the inversion center.

Structural models were refined by the Rietveld method using the FULLPROF program [34]. A total of 46 and 52 intensity-dependent parameters for **(1)** and **(2)**, **(3)**, respectively, including

Table 1
Crystal data and structure refinement parameters

Compound	**(1)** $Ni_5(OH)_6(C_6H_8O_4)_2$	**(2)** $Ni_5(OH)_6(C_8H_{12}O_4)_2$	**(3)** $Co_5(OH)_6(C_8H_{12}O_4)_2$
Fw (g/mol)	683.75	739.84	741.05
System	Triclinic $P-1$	Triclinic $P-1$	Triclinic $P-1$
a (Å)	11.6504(1)	13.9325(1)	13.9806(1)
b (Å)	6.8021(3)	6.7893(1)	6.9588(1)
c (Å)	6.3603(1)	6.3534(4)	6.3967(1)
α (°)	73.52(1)	73.63(1)	73.05(1)
β (°)	99.69(1)	95.14(1)	94.51(1)
γ (°)	96.16(1)	91.80(1)	92.19(1)
V (Å^3)	475.491(4)	574.288(6)	593.375(10)
Z	1	1	1
Colour	Green	Green	Pink
Dx (g/cm^3)	2.387	2.137	2.0738
Wave length (Å)	0.85124	0.85124	0.85124
Absorption coefficient ($\mu \times r$)	3.87	3.21	2.53
2θ range (deg)	1.59–42.96	1.71–42.96	1.81–32.96
N obs of points	13789	13751	10384
N_{ref}	668	804	410
Rp	0.069	0.065	0.045
Rwp	0.114	0.094	0.073
χ^2	5.003	5.97	5.248
R_{Bragg}	0.070	0.052	0.048
R_F	0.091	0.097	0.083
N profile parameters	32	19	32
N intensity dependent parameters	46	52	52
N constraints	31	35	35
Excluded regions (°)	10.0–10.78	–	4.5–6.00 10.74–10.92

the atoms coordinates and an overall thermal displacement were refined. The following soft geometrical constrains have been applied on the organic molecules during the refinement: C–C = 1.54(1) Å, C–O = 1.26(1) Å; C–C–C = 110.0(2)° (13 and 17 soft constrains for adipate and subarate molecules, respectively). Additionally, for each structure, soft constrains on the three *M*O6 octahedra were also applied: Ni–O = 2.10(1) Å for **(1)** and **(2)**, and Co–O = 2.15(2) Å for **(3)**. Consequently, 31 (13+18) constraints were used in **(1)** and 35 (17+18) in **(2)** and **(3)**. The 2θ ranges, 10.0–10.78° corresponding to the main line of the impurity identified as $Ni(OH)_2$ (PDF 14–117) in **(1)**, 4.50–6.00° and 10.74–10.92° corresponding to an unidentified impurity in **(3)** were excluded from the refinements. The observed, calculated and difference patterns are compared in Fig. 2 and the fractional atomic coordinates are reported in Supplementary material in Tables SI–III for **(1)**, **(2)** and **(3)**. Interatomic distances were calculated using the Fullprof program.

3. Results and discussion

3.1. Spectroscopy results

The FT-IR spectra shown in Fig. 3 for **(1)**, **(2)** and **(3)** are very similar. Two intense bands at 1564 and 1407 cm^{-1} were assigned to stretching υ_{as}(–COO–) and υ_s(–COO–), respectively. The difference between these two bands ($\Delta\nu = 155$ cm^{-1}) agrees with a bridging character of the $-COO^-$ groups, with two oxygen atoms linked to Ni^{II} or Co^{II}. Three bands around 2930 cm^{-1} correspond to different stretching modes of the H–C–H group. The bands observed in the 3600–3500 cm^{-1} range correspond to the stretching of the OH groups.

The UV spectra are reported in Fig. 4. For the nickel-based compounds **(1)** and **(2)**, the bands observed towards 700 and 390 nm correspond to electronic transitions from the fundamental state $A_{2g}(F)$ towards the excited states $^3T_{1g}$ (υ_2) and $^3T_{1g}(P)$ (υ_3) of a nickel atom in octahedral coordination. For **(3)**, the band at about 500 nm corresponds to the transition $^4T_{1g}(F) \rightarrow {}^4A_{2g}(F)$ in case high-spin Co^{2+} is located in octahedral geometry.

3.2. Structure description

As the structures of **(1)**, **(2)** and **(3)** are very close, only that of **(2)** is presented in Fig. 5. All the structures are formed by layers connected by dicarboxylates anions. They differ mainly either by the nature of the metal cation or by the inter-layer distance d_0 ($d_0 = 11.43$, 13.93 and 13.86 Å for **(1)**, **(2)** and **(3)**, respectively), which is related to cell parameter a (see Table 1). The Ni^{2+} and Co^{2+} cations are coordinated by six O atoms (four O atoms from hydroxide and two O atoms from the bidentate bridging carboxylate) in an octahedral arrangement, in agreement with the UV spectra.

Selected interatomic distances are reported in Table 2. Average *M*–O distances in the three compounds are *M*(1)–O = 2.091 Å in **(1)**, 2.062 Å in **(2)** and 2.135 Å in **(3)**; *M*(2)–O = 2.062 Å in **(1)**, 2.060 Å in **(2)** and 2.145 Å in **(3)** *M*(3)–O = 2.071 Å in **(1)**, 2.034 Å in **(2)** and 2.102 Å in **(3)**, in line with the sum of the ionic radii given by the Shannon table ($rNi^{2+} = 0.69$ Å, $rCo^{2+} = 0.745$ Å (HS), $rO^{2-} = 1.40$ Å). The C–C($\approx$1.55 Å), C–O($\approx$1.25 Å) distances and C–C–C($\approx$110°), C–O–C ($\approx$122°) angles are close to the expected values.

The layers are built from edge-sharing octahedra and exhibit pores that can be seen as apertures of channels running along [111]. Their average diameter estimated for the O–O distance is ~4.5 Å, which is probably too small to generate absorption properties. The microporous aspect of the slabs is represented in Fig. 6. The condensation of the '*M*O6' octahedra observed in **(1)**, **(2)** or **(3)** is quite uncommon, to our knowledge. It is presented in Fig. 7. The connection of five octahedra of the unit formula '$(M2)_2(M1)(M3)_2$' forms a cross-like unit: the central *M*1 octahedron sits on an inversion center while the horizontal and vertical branches are formed by the *M*3 and *M*2 octahedra, respectively. *M*3 and *M*2 are connected to *M*1 through their four equatorial

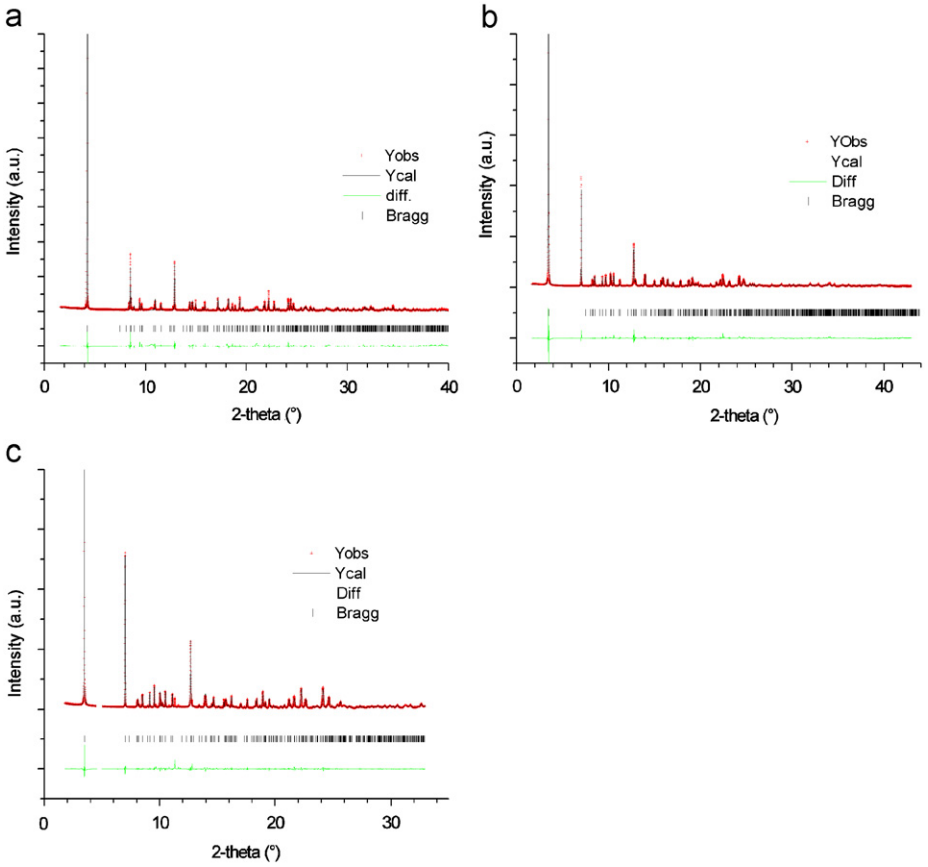

Fig. 2. Observed, calculated and difference XRPD pattern for **(1)**, **(2)** and **(3)**.

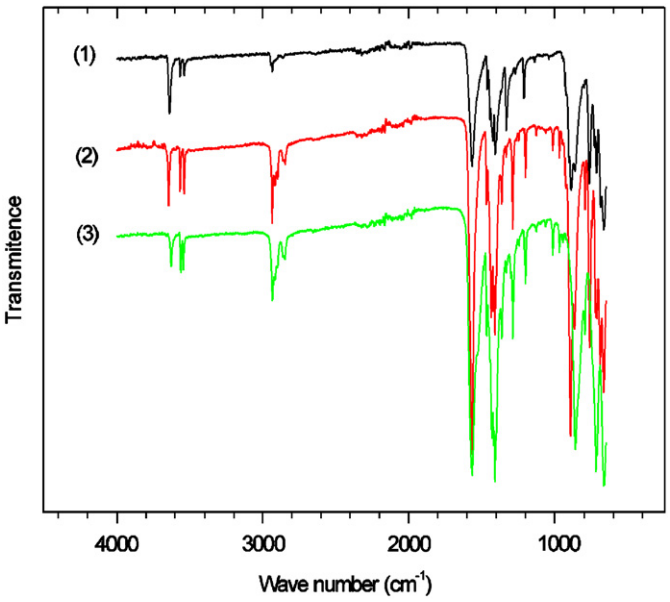

Fig. 3. FT-IR spectrum of **(1)**, **(2)** and **(3)**.

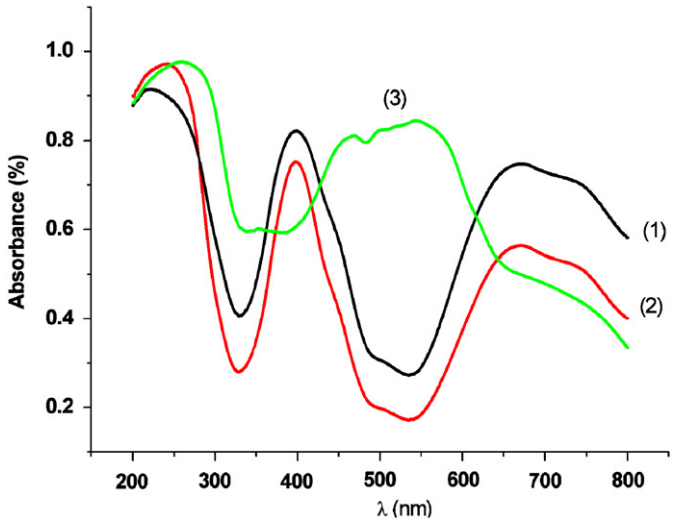

Fig. 4. UV–visible spectra of **(1)**, **(2)** and **(3)**.

edges. The connection of two cross-like units by edges, which are out of the equatorial plane of the central *M*1 octahedron, leaves a free space or hole as can be seen in Fig. 7. It is different from the connection of the four equatorial edges of octahedra leading to the brucite layer. The brucite layers do not present any holes. Due to this connection mode of the octahedra in **(1)**, **(2)** and **(3)**, holes are formed, which are the smallest that can be generated by edge-sharing octahedra. This contrasts with some open structures observed for other layered hydroxy–dicarboxylate materials that exhibit pores with a size up to tens of Angströems [20,25].

3.3. Magnetic properties

Compounds **(1)** and **(2)** have similar magnetic behaviors as can be seen in Figs. 8 and 9, respectively. In both cases, the χT product continuously decreases upon cooling (from 4.50 cm^3 K/mol at 300 K down to 1.97 cm^3 K/mol at 27 K for **(1)** and from 3.29 cm^3 K/mol at 300 K down to 0.62 cm^3 K/mol at 19 K for **(2)**), which is a clear

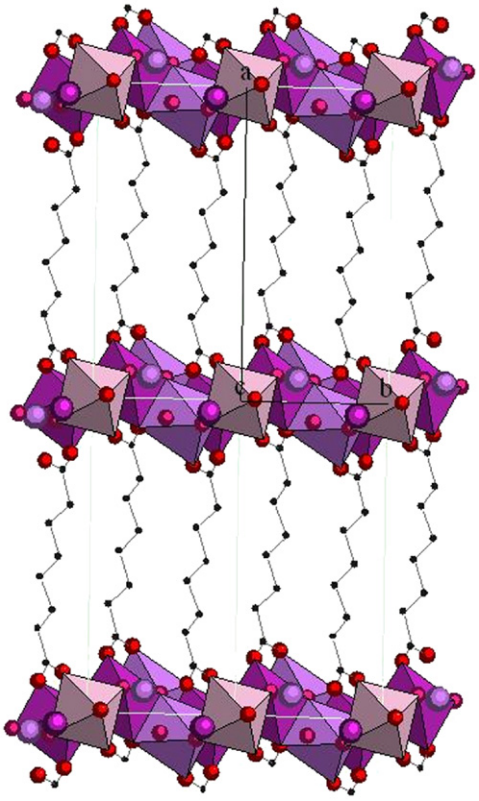

Fig. 5. General view of the layered structure of **(2)** and **(3)** in projection along the *c*-axis. The structure of **(1)** is similar but with six carbon atoms for the aliphatic chains.

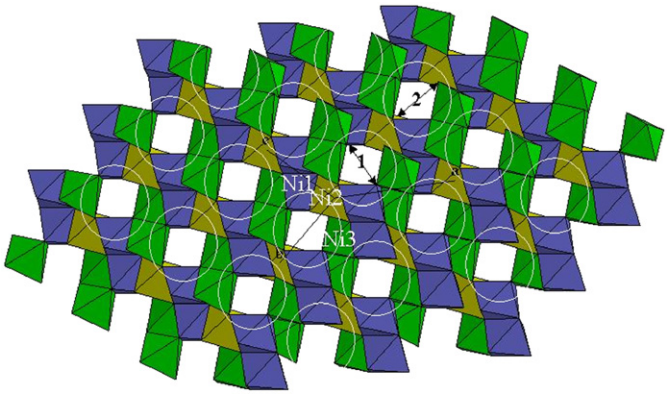

Fig. 6. Representation of one layer showing the pores.

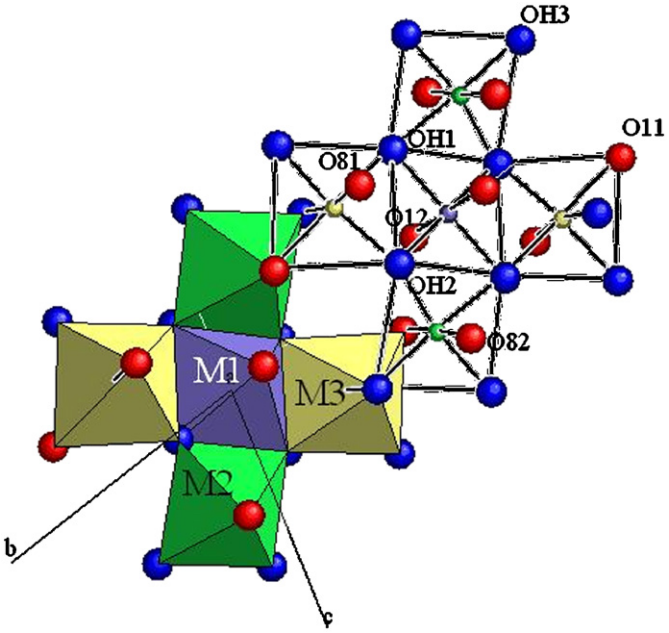

Fig. 7. View showing the edge-sharing octahedra into and between two cross-like units $M_5(OH)_6(O_2CC_nH_{2n}CO_2)_2$. Carbon and H atoms are not represented.

Table 2
Selected interatomic distances (Å) and angles (°) in **(1)**, **(2)** and **(3)**

$Ni_5(OH)_6(C_6H_8O_4)_2$ **(1)**		$Ni_5(OH)_6(C_8H_{12}O_4)_2$ **(2)**		$Co_5(OH)_6(C_8H_{12}O_4)_2$ **(3)**	
Atom–atom	Distances (Å)	Atom–atom	Distances (Å)	Atom–atom	Distances (Å)
Ni1–O12	2 × 2.079(9)	Ni1–O12	2 × 2.034(9)	Co1–O12	2 × 2.107(8)
Ni1–OH1	2 × 2.100(5)	Ni1–OH1	2 × 2.067(6)	Co1–OH2	2 × 2.115(8)
Ni1–OH2	2 × 2.065(9)	Ni1–OH2	2 × 2.045(8)	Co1–OH1	2 × 2.071(4)
Ni2–O11	2.065(9)	Ni2–O11	2.049(9)	Co2–O11	2.089(8)
Ni2–O62	2.039(9)	Ni2–O82	2.064(9)	Co2–O82	2.119(8)
Ni2–OH1	2.181(8)	Ni2–OH1	2.182(9)	Co2–OH1	2.191(6)
Ni2–OH1	2.063(8)	Ni2–OH1	2.065(7)	Co2–OH1	2.081(6)
Ni2–OH2	2.076(9)	Ni2–OH2	2.034(8)	Co2–OH2	2.111(8)
Ni2–OH3	2.133(9)	Ni2–OH3	2.039(9)	Co2–OH3	2.128(8)
Ni3–O11	2.13(1)	Ni3–O11	2.11(1)	Co3–O11	2.110(9)
Ni3–O61	2.08(1)	Ni3–O81	2.09(1)	Co3–O81	2.161(9)
Ni3–OH1	2.176(8)	Ni3–OH1	2.188(9)	Co3–OH1	2.234(7)
Ni3–OH2	2.066(7)	Ni3–OH2	2.052(6)	Co3–OH2	2.069(6)
Ni3–OH3	2.048(8)	Ni3–OH3	2.028(8)	Co3–OH3	2.041(8)
Ni3–O3	2.080(8)	Ni3–OH3	1.993(9)	Co3–OH3	2.120(7)
C1–C2	1.57(2)	C1–C2	1.59(1)	C1–C2	1.569(9)
C2–C3	1.55(2)	C2–C3	1.53(2)	C2–C3	1.55(2)
C3–C4	1.55(2)	C3–C4	1.52(1)	C3–C4	1.55(1)
C4–C5	1.55(2)	C4–C5	1.54(2)	C4–C5	1.55(2)
C5–C6	1.58(2)	C5–C6	1.55(1)	C5–C6	1.55(1)
C1–O11	1.25(2)	C6–C7	1.56(2)	C6–C7	1.56(2)
C1–O12	1.26(2)	C7–C8	1.58(1)	C7–C8	1.565(8)
C6–O61	1.27(2)	C1–O11	1.33(2)	C1–O11	1.30(2)
C6–O62	1.26(2)	C1–O12	1.28(2)	C1–O12	1.30(1)
		C8–O81	1.28(2)	C8–O81	1.28(2)
		C8–O82	1.30(2)	C8–O82	1.29(1)

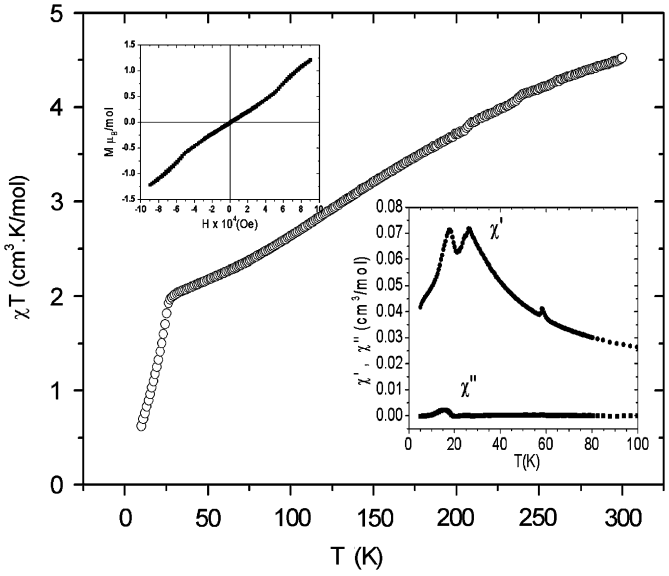

Fig. 8. χT product and χ_{AC} (lower inset) vs. temperature and magnetization vs. field (upper inset) in **(1)**.

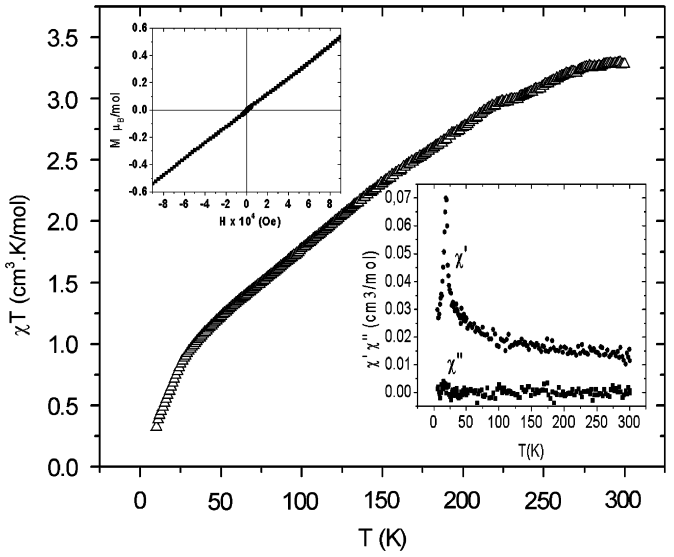

Fig. 9. χT product and χ_{AC} (lower inset) vs. temperature and magnetization vs. field (upper inset) in **(2)**.

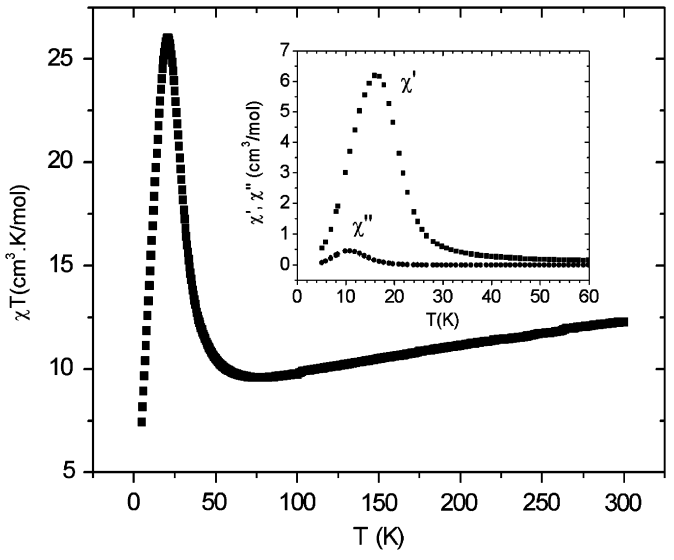

Fig. 10. χT product and χ_C (inset) vs. temperature in **(3)**.

signature of 2D antiferromagnetic interactions. A fit of the reciprocal susceptibility $1/\chi$ in the high-temperature range (ca. 120–300 K) using the Curie–Weiss law yields the following paramagnetic Curie temperatures and Ni(II) effective moments: $\theta_p = -228$ K and $\mu_{eff.} = 3.34\,\mu_B$ for **(1)** and $\theta_p = -249$ K and $\mu_{eff.} = 3.12\ \mu_B$ for **(2)**. Such θ_p values are indicative of strong in-plane antiferromagnetic interactions while the $\mu_{eff.}$ values are close to the~$3.2\,\mu_B$ expected for the Ni^{2+} ion. At $T_N = 27$ K for **(1)** and $T_N = 19$ K for **(2)**, the rate of decrease of χT with temperature significantly increases, in a more pronounced manner for **(1)**, suggesting a 3D antiferromagnetic ordering of the Ni moments. This is corroborated by the AC susceptibility measurements (inset of Figs. 8 and 9) characterized by a peak in χ' at these temperatures without the corresponding peak in the out-of-phase signal. Note that the anomalies observed at 18 K in the thermal dependence of the AC susceptibility of **(1)** is unambiguously due to a small amount of the $Ni(OH)_2$ ferromagnetic impurity detected in the powder X-ray diffraction patterns. The peak in χ' of **(1)** observed at ~60 K is an arte fact as it was not reproduced on other magnetic curves (not shown here). The higher ordering temperature of **(1)** likely results from its lower inter-layer

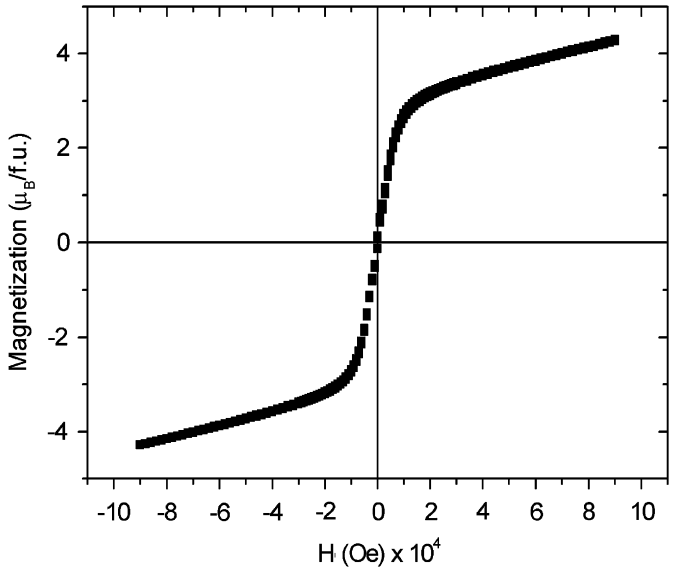

Fig. 11. Field-dependent magnetization in **(3)** at 5 K.

spacing. The main difference between the magnetic properties of **(1)** and **(2)** is found in the field dependence of their magnetization at 5 K (inset of Figs. 8 and 9): that of **(2)** is a straight line, as expected for a simple antiferromagnet, whereas the $M(H)$ curve of **(1)** shows a weak and almost anhysteretic field-induced transition at a threshold field of 50 kOe.

The magnetic behavior of **(3)** is quite different. The χT product first decreases upon cooling (Fig. 10) from 12.3 cm^3 K/mol at room temperature down to a minimum of 9.6 cm^3 K/mol at 74 K and then goes to a sharp maximum at 20.8 K before decreasing rapidly at lower temperatures. The decrease of χT upon cooling between 300 and 74 K points to 2D antiferromagnetic interactions. Spin–orbit effects might also partially contribute. The fit of the reciprocal susceptibility above 90 K gives $\theta_p = -15$ K and an effective Co(II) magnetic moment value of 4.42 μ_B, close to that expected for a high-spin Co^{2+} ion. The sharp increase in χT at lower temperatures is characteristic of a magnetized 3D magnetic order, in agreement with the existence of an out-of-phase signal in the temperature dependence of AC susceptibility (inset of Fig. 10). Compound **(3)** is thus a ferrimagnet (or equivalently a canted uncompensated antiferromagnet) below $T_C = 16.3$ K. The field dependence of the magnetization $M(H)$ recorded at 5 K (Fig. 11) does not reveal any significant hysteresis. It shows that above about 20 kOe the magnetization still increases significantly linearly, likely due to the decrease of the canting angle between the Co(II) moments, and is far from saturation even at 90 kOe, where the magnetization M per formula unit (i.e. for five Co atoms) reaches $M = 4.27\,\theta_B$/f.u.

4. Conclusions

Three new hybrid compounds in the system M(II)–OH-linear dicarboxylates synthesized by the hydrothermal route in basic media base have been found (M = Ni, Co). Their structures have been solved *ab initio* from powder synchrotron data. All the structures are layered, with bidendate carboxylate groups covalently grafted to the M–OH layers and acting as a spacer. The layers are built from edge-sharing M(II)O6 octahedra, with an original connection scheme that leads to the formation of very small channels with about 4 Å of aperture running along [111]. The two Ni-based compounds (**(1)** and **(2)**) are antiferromagnets while the Co-based one **(3)** is ferrimagnetic. Since the crystal structures

are very close, this difference is likely linked to the nature of the magnetic orbitals (e_g for Ni^{2+}; e_g and t_{2g} for Co^{2+}).

Supporting material

Crystallographic data (excluding structure factors) for the structure(s) reported in this paper have been deposited with the Cambridge Crystallographic Data Centre as supplementary publication no. CCDC_652775–652777.

Copies of the data can be obtained free of charge on application to CCDC, 12 Union Road, Cambridge CB2 1EZ, UK (fax: +44 1223 336 033; e-mail: deposit@ccdc.cam.ac.uk).

Acknowledgment

The authors would like to thank Irena Margiolaki (European Synchrotron Radiation Facilities (ESRF)' in Grenoble, France) for her help during the experiments.

Appendix A. Supplementary materials

Supplementary data associated with this article can be found in the online version at doi:10.1016/j.jssc.2008.06.059.

References

[1] D. Maspoch, D. Ruiz-Molina, J. Veciana, Chem. Soc. Rev. 36 (2007) 770.
[2] S. Kitagawa, R. Kitaura, S.-I. Noro, Angew. Chem. Int. Ed. 43 (2004) 2334.
[3] C. Sanchez, G.J. de, A.A. Soler-Illia, F. Ribot, T. Lalot, C.R. Mayer, V. Cabuil, Chem. Mater. 13 (2001) 3061.
[4] G. Férey, Chem. Mater. 13 (10) (2001) 3084.
[5] J.L.C. Rowsell, O.M. Yaghi, Angew. Chem. Int. Ed. 44 (2005) 4670.
[6] C.N.R. Rao, S. Natarajan, R. Vaidhyanathan, Angew. Chem. Int. Ed. 43 (2004) 1466.
[7] P. Rabu, M. Drillon, Adv. Eng. Mater. 5 (4) (2003) 189.
[8] N. Guillou, C. Livage, G. Férey, Eur. J. Inorg. Chem. (2006) 4963.
[9] J.M. Rueff, J.F. Nierengarten, P. Gilliot, A. Demessence, O. Cregut, M. Drillon, P. Rabu, Chem. Mater. 16 (2004) 2933.
[10] N. Guillou, S. Pastre, C. Livage, G. Férey, Chem. Commun. (2002) 2358.
[11] S. Konar, P.S. Mukherjee, E. Zangrando, F. Lloret, N.R. Chaudhuri, Angew. Chem. Int. Ed. 41 (9) (2002) 1561.
[12] Y.-Q. Zheng, H.-Z. Xie, J. Solid State Chem. 177 (2004) 1352.
[13] N. Guillou, C. Livage, W. Van Beek, M. Noguès, G. Férey, Angew. Chem. Int. Ed. 42 (6) (2003) 643.
[14] C. Serre, F. Millange, C. Thouvenot, M. Noguès, G. Marsolier, D. Louër, G. Férey, J. Am. Chem. Soc. 124 (2002) 13519.
[15] D.T. Tran, X. Fan, D.P. Brennan, P.Y. Zavalij, S.R.J. Olivier, Inorg. Chem. 44 (18) (2005) 6192.
[16] Z.L. Huang, M. Drillon, M. Masciocchi, A. Sirani, J.T. Zhao, P. Rabu, P. Panissod, Chem. Mater 12 (2000) 2805.
[17] M. Kurmoo, H. Kumagai, M.A. Greeen, B.W. Lovett, S.J. Blundell, A. Ardavan, J. Singleton, J. Solid State Chem. 159 (2001) 343.
[18] R. Feyerherm, A. Loose, P. Rabu, M. Drillon, Solid State Sci. 5 (2003) 321.
[19] S. Abdelouhab, M. François, E. Elkaim, P. Rabu, Solid State Sci. 7 (2005) 227–232.
[20] C. Livage, C. Egger, M. Nogues, G. Férey, J. Mater. Chem. 8 (1998) 2743.
[21] Y.J. Kim, D.-Y. Jung, Bull. Korean Chem. Soc. 20 (7) (1999) 827.
[22] Y.J. Kim, D.-Y. Jung, K.-P. Hong, G. Demazeau, Solid State Sci. 3 (2001) 837.
[23] Y.-Q. Zheng, J. Sun, J. Solid State Chem. 172 (2003) 288.
[24] M. Kurmoo, J. Mater. Chem. 9 (1999) 2595.
[25] C. Livage, C. Egger, G. Férey, Chem. Mater. 11 (1999) 1546.
[26] P.M. Forster, A.K. Cheetham, Angew. Chem. Int. Ed. 41 (3) (2002) 457.
[27] M. Drillon, P. Panissod, J. Magn. Magn. Mater. 188 (1998) 93.
[28] M. Kurmoo, H. Kumagai, S.M. Hughes, C.J. Kepert, Inorg. Chem. 42 (2003) 6709.
[29] 〈http://www.qdusa.com〉.
[30] A.N. Fitch, J. Res. Natl. Inst. Stand. Technol. 109 (2004) 33–142.
[31] 〈http://www.accelrys.com/products/mstudio/modeling/crystallization/reflex.html〉.
[32] A.M.J. Neumann, Appl. Crystallogr. 36 (2003) 356.
[33] V. Favre-Nicolin, R. Cerny, Z. Kristallogr. 219 (2004) 847.
[34] J. Rodriguez-Carvajal, M.T. Fernandez-Diaz, J.L. Martinez, J. Phys.: Condens. Matter 3 (1991) 3215.